Inclusive cross sections for pion and proton production by photons using collimated coherent bremsstrahlung*

W. Kaune,† G. Miller,‡ W. Oliver, R. W. Williams, and K. K. Young
Department of Physics, University of Washington, Seattle, Washington 98195
(Received 13 May 1974)

Cross sections for the inclusive processes $\gamma p \to \pi^{\pm} X$ and pX have been measured at the Stanford Linear Accelerator Center for linearly polarized photons of average energy 10 and 14 GeV. The kinematic range of detected particles was $P_T = 0.15$ to 1.0 GeV/c, $x = 0$ to -0.32 for pions and -0.3 to -0.8 for protons at 10 GeV; the 14-GeV data had measurements at $x = 0$ for pions and $x \approx -0.3$ for protons. The experiment was carried out using collimated coherent bremsstrahlung from a thin diamond radiator and the SLAC 1.6-GeV/c spectrometer. The variation of the cross section, as a function of x and P_T, shows a marked similarity to that observed for pion and proton production from pp collisions. Our results show little dependence of the pion invariant cross section on either energy or polarization. The π^+/π^- ratio varies from 1.3 at $x = 0$ to 1.75 at $x = -0.32$.

I. INTRODUCTION

A prominent feature of multiparticle production in high-energy collisions has been the approximate "projectile independence" of the spectra of particles produced at low energy in the rest frame of the target proton (the target fragmentation kinematical region). Earlier work[1,2] has shown that the cross sections for $ap \to \pi^- X$ where a is p, π^-, π^+, K^+, or γ, when integrated over the transverse momentum, are very similar in the target fragmentation region. A scarcity of high-statistics data[3] in all but the p-p reaction so far has severely restricted comparisons of the differential cross sections.

We report here a measurement of the inclusive cross section, $Ed\sigma/d^3p(k, x, P_T)$ for $\gamma p \to cX$ where c is p, π^+, and π^-. We have chosen as kinematic variables the transverse momentum P_T, the fractional center-of-mass longitudinal momentum x calculated in terms of the incoming photon (or proton) momentum, and the photon energy k. The mean photon energy was 10 GeV for the bulk of the data and 14 GeV for the remainder.

The experiment was performed at the Stanford Linear Accelerator (SLAC) using a novel, effectively monochromatic, high-energy photon beam produced by tightly collimating a coherent bremsstrahlung beam. This technique was an essential feature of the experiment. In a conventional bremsstrahlung photon beam, the yield of low-energy secondaries which we detected would have been completely dominated by production from low-energy photons. This would have made the extraction of good quality high-energy data quite difficult. The photon beam was polarized, thus allowing a measurement of the polarization dependence of the cross sections. The secondary particles were detected in the SLAC 1.6-GeV/c spectrometer, using a threshold Čerenkov counter for particle identification.

We have compared the cross sections for p, π^+, and π^- production in the target fragmentation region with the parallel cross sections for p-p reactions. These cross sections are remarkably similar in detail for such different species of projectiles, even at these relatively low energies. Our data are consistent with no change in cross section to within ±10% from 10 to 14 GeV at $x = 0$ and with no polarization dependence of the $\pi^{\pm}$ cross section to within ~6%. At some points the proton data show a 10–20% polarization asymmetry. The π^+/π^- ratio, always >1, increases as x becomes more negative.

II. DESCRIPTION OF THE EXPERIMENT

A. Experimental arrangement

The experiment was performed in the *"A"* electron beam line at SLAC. The design, construction, and testing of the photon beam were done in collaboration with members of the SLAC Spectrometer Facilities Group; a detailed description is in preparation.[4] The layout of the experimental apparatus is shown in Fig. 1.

The source of the photon beam was a thin (80 μ thick) diamond crystal inserted in the electron beam line 95 m upstream of the spectrometer pivot point in end station A. The primary photon collimator was a 2-mm-diameter-bore, 70-radiation-length-long tungsten cylinder 91 m downstream of the diamond. The electron beam transport sys-

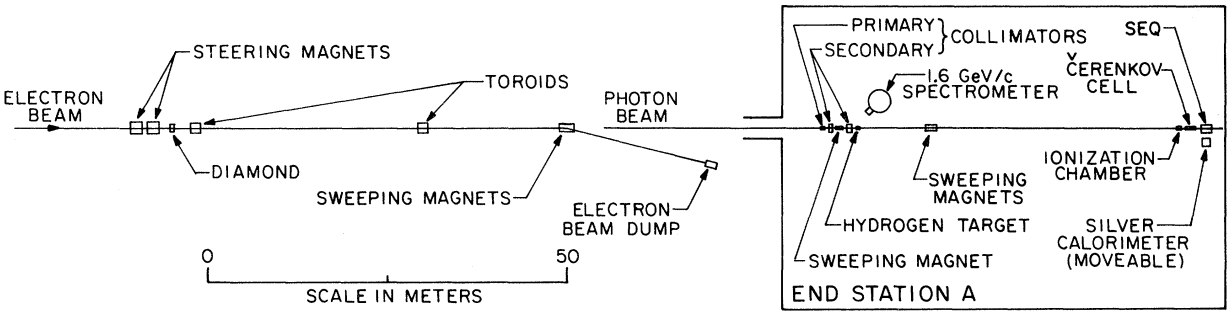

FIG. 1. Schematic plan view of the experimental layout. The electron beam dump was actually below the photon beam.

tem was designed to image (with a demagnification of 3) a 6×6-mm aperture at the end of the accelerator onto the aperture of the collimator. The central electron momentum was 19.7 GeV/c, defined by a slit set for a full width of 0.5%.

The diamond was mounted in a two-axis goniometer and could be oriented by remote control. The goniometer was originally used in an uncollimated coherent bremsstrahlung beam built by a SLAC-MIT collaboration.[5] It allows orientation of the diamond in steps of 23 μrad about either axis. The range of allowed angles is ~120 mrad. Collimators 22 m upstream of the goniometer and around a bend of 6° were positioned to prevent the electron beam from striking the diamond holder. Fine control of the electron beam steering was provided by two dipole magnets immediately upstream of the goniometer. The electron beam intensity was monitored at two positions near the goniometer by SLAC "toroids,"[5] which are well-understood precision beam monitors.

Dipole magnets 50 m downstream of the diamond deflected the electron beam down into a beam dump. The photon beam proceeded on to the primary collimator. Immediately upstream of the collimator and housed in the same assembly was a four-quadrant tungsten-pin shower-emission detector[6] used as a beam-position monitor. The assembly could be rotated about the beam through 180° to allow balancing of opposite quadrants. The primary collimator was followed by a 6.35-mm-diameter-bore, 0.38-m-long copper collimator, a 7-kG-m dipole magnet sweeping vertically, and a 12.7-mm-diameter-bore, 0.51-m-long lead collimator. The secondary collimation removed charged particles from the beam and shielded the hydrogen target and its surrounding structures from particles originating in the primary collimator.

The hydrogen target was centered on the spectrometer pivot point. The target cell was a 1-cm-diameter, 30-cm-long Mylar tube with 0.005-in.-thick walls and 0.001-in.-thick aluminum end caps. The full target cell could be replaced by a similar empty cell by remote control.

Charged particles produced in the hydrogen target were detected with the SLAC 1.6-GeV/c spectrometer.[7] We operated the spectrometer over a range of angles from 18° to 85° and over a momentum range from 0.5 to 1.5 GeV/c.

The photon beam monitor was a total-absorption secondary-emission quantameter (SEQ) (see Ref. 8) 50 m downstream of the hydrogen target. Immediately upstream of the SEQ were two auxiliary beam monitors: a thin-foil hydrogen-filled ionization chamber and a 1-atm air-filled Čerenkov cell. Dipole magnets 10 m downstream of the hydrogen target deflected charged particles out of the transmitted photon beam.

B. Beam monitors

The spectrum of the transmitted photon beam depends sensitively on the centering of the beam on the collimator aperture. Hence it was necessary to monitor the photon beam on a pulse-by-pulse basis to be able to reject photon pulses originating from a missteered beam. The signals from the three beam-intensity monitors as well as from the four quadrants of the beam-position monitor were integrated over the 1.6-μsec SLAC pulse by means of charge-sensitive amplifiers. The outputs of the amplifiers, converted to digital form, were read into the computer for every pulse.

Each quadrant of the beam-position monitor had a sensitive area of 9.0 mm^2 at a mean radius of 3.3 mm. After each beam pulse the on-line computer calculated the asymmetries for the two pairs of opposite quadrants. The computer was programmed to analyze the asymmetry data and, if necessary, to resteer the beam by altering the currents in trim windings on the two dipole magnets immediately upstream of the goniometer. We did not accept data unless the beam was centered to within 0.15 mm in both planes. During stable operation of the accelerator virtually all the beam pulses satisfied this criterion.

The energy in the photon beam was monitored by integrating the current from the SEQ with an integrating digital voltmeter. The charge corresponding to the subset of properly steered pulses was determined from the summed pulse-by-pulse readouts of the SEQ. The relation between the accumulated charge and the energy deposited in the SEQ was determined by comparing, in calibration runs, the output on the SEQ with that of the SLAC silver calorimeter. The mean calibration constant obtained was 3.06×10^{-7} pC/GeV. The measurements of the calibration constant agreed to within 2% over the course of the experiment.

C. 1.6-GeV/c spectrometer

The spectrometer is a 100-in.-radius, 90°-vertical-bend, essentially uniform field magnet.[7] The entrance and exit pole faces are canted to produce a parallel-to-point focus in the nonbend plane while retaining the point-to-point focus in the bend plane. Both foci occur in a horizontal plane 100 in. above the exit of the magnet. The spectrometer and associated counters are shown in Fig. 2.

The momentum acceptance and the acceptance in production angle (projected on the horizontal plane) were defined by hodoscopes designated P and θ at the focal plane. The acceptance was 9.9%

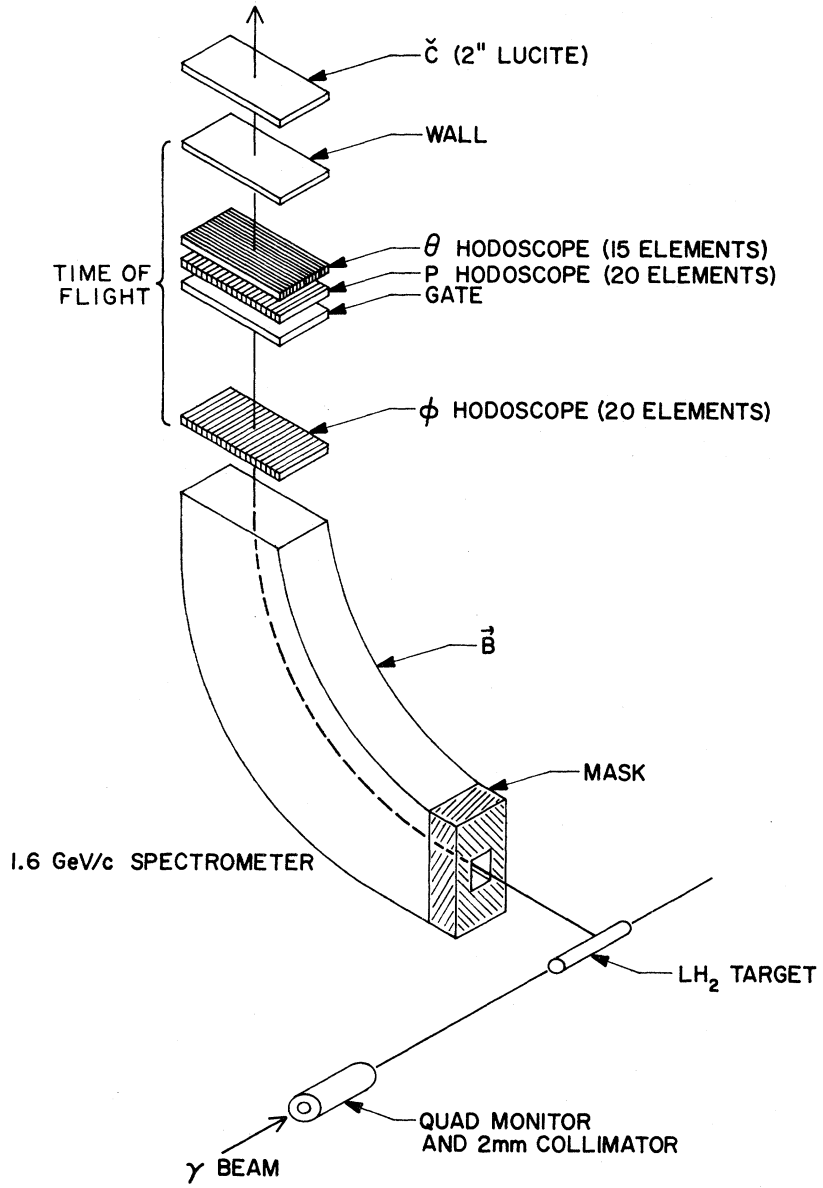

FIG. 2. Schematic view of the SLAC 1.6-GeV/c spectrometer as instrumented for this experiment.

in the momentum. The vertical extent of the entrance aperture limited the acceptance in azimuthal angle to a total of 60 mrad. The 6-in. width of the aperture, together with the full 33.6-mrad acceptance of the θ hodoscope, determined the acceptance in production angle, and also, except at the most forward angles, the effective target length. The hodoscope designated ϕ, 41 in. above the magnet exit, provided redundant information on the azimuthal angle. The resolution of our hodoscope system was calculated to be about $\pm 0.25\%$ in momentum, ± 1.1 mrad in production angle, and ± 7.5 mrad in azimuthal angle.

We triggered our electronics on a coincidence between two scintillation counters ("gate" and "wall" in Fig. 2) located near the focal plane. The trigger counters were oversize to insure that the acceptance was set by the P and θ hodoscopes. When a trigger occurred we read in all hodoscope elements as well as the pulse heights of the 0.25-in.-thick gate counter, the 0.375-in.-thick wall counter, and the 2-in.-thick Lucite Čerenkov counter.

The Čerenkov counter provided the principal means of particle identification. It was observed to be nearly 100% efficient for 0.3-GeV/c pions ($\beta = 0.91$) and almost totally inefficient for 1.5-GeV/c protons ($\beta = 0.85$). The calculated threshold velocity, 0.89, gives a kaon threshold of 1.0 GeV/c. Pulse heights from the wall counter and time-of-flight (TOF) information between the ϕ hodoscope and the wall counter were useful for checks at low-momentum settings. The TOF system had a flight path of 180 cm and a full width at half maximum (FWHM) resolution of ± 1.5 nsec. A sample TOF distribution is shown in Fig. 3.

III. EXPERIMENTAL METHOD

A. Photon beam

Here we discuss the use of collimated coherent bremsstrahlung (CCB) to produce an effectively monochromatic and linearly polarized photon beam. We first give a short description of the general principles involved, and then explain the method used to measure inclusive cross sections with this beam.

In bremsstrahlung, for high energy of the incoming electron, the momentum transfer $|\vec{q}| = q$ to the radiator material tends to be very small. As a result it becomes quite probable that the radiator will not change state, and coherent radiation from a crystal becomes possible. Energy transfer to the crystal is negligibly small, in that case, and the equations of momentum and energy conservation lead to the following approximate relation:

$$q_z = \frac{m^2 k(1 + E^2\theta^2/m^2}{2E(E-k)} \quad . \tag{1}$$

Here q_z is the component of the momentum transfer to the crystal along the electron beam direction, m the electron mass, E the incoming electron energy, k the photon energy, and θ the photon angle with respect to the incoming electron beam direction. Equation (1) with $\theta = 0$ gives the minimum value of q_z, which is also the minimum q necessary if an electron radiates a photon of energy k. For values typical of our experiment, $E = 20$ GeV and $k = 10$ GeV, $q_{z\,\min} \approx 6$ eV/c.

A generalized Bragg relation[9] connects "recoilless" momentum transfer with crystal structure. The probability for coherent radiation is nonzero only for $\vec{q}$ equal to one of the reciprocal lattice vectors of the crystal. The smallest momentum transfer that can be taken up coherently by a diamond crystal corresponds, because of some cancellations, to $2\pi\sqrt{8}$ times the reciprocal lattice constant, or a momentum of 10 keV/c, so the direction of $\vec{q}$ is very nearly transverse to the electron beam.

For each reciprocal lattice vector $\vec{q}$, Eq. (1) implies a relation between energy k and angle θ of the radiated coherent photons, neglecting the slight angular divergence of the electron beam. This energy-angle constraint was exploited by limiting the angle θ by collimation about the electron beam direction, producing nearly monochromatic spikes in the energy spectrum. The energy of the leading edge of a particular spike is given

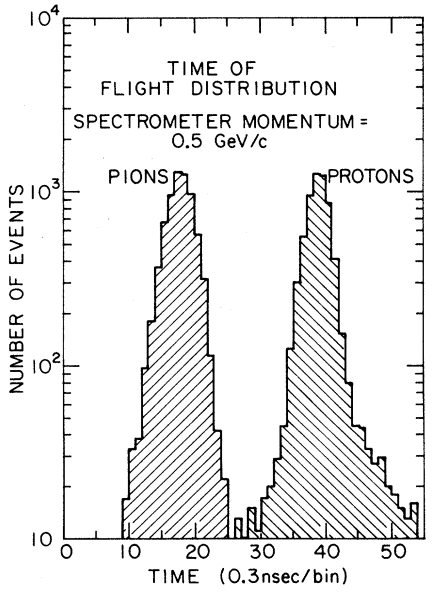

FIG. 3. Typical time-of-flight distribution; spectrometer momentum 0.5 GeV/c.

by Eq. (1), setting $\theta = 0$.

At SLAC energies, the collimation angle must be very small. For the electron beam energy used in this experiment, 19.7 GeV, m/E is 26×10^{-6}. The collimation angle was 11×10^{-6} rad. Actually the collimation was not sharply defined, but was effectively smeared out by multiple scattering of the electron beam in the diamond and electron beam spot size effects. Some photons with an angle of m/E or larger were accepted. A detailed treatment is given in Appendix A.

Reciprocal lattice vectors with the smallest indices h, k, l and hence the smallest q are the most important in the bremsstrahlung process. Of these, only ones nearly perpendicular to the initial beam direction and therefore having small q_z give prominent spikes. For a nonsimple lattice such as diamond, certain reciprocal lattice vectors give zero contribution because of a cancellation of the bremsstrahlung amplitude within each unit cell. In diamond the general rule for allowed reciprocal lattice vectors (h, k, l) with $h = 0$ is the following: k, l even, $k + l$ divisible by 4. The smallest allowed reciprocal lattice vectors are the following: (0, 2, 2), (0, 0, 4), (0, 2, 6), (0, 0, 8), (0, 6, 6), . . . , where lattice vectors symmetrically located about the (1, 0, 0) direction are naturally included, that is, (0, ±4, 0) and (0, 0, −4) as well as (0, 0, 4), for example. Generally only the (0, 2, 2), (0, 4, 4), (0, 6, 6), and (0, 8, 8) reciprocal lattice vectors were needed to approximate the coherent spectrum, with the most prominent contribution coming from the (0, 2, 2).

A calculated spectrum is shown in Fig. 4 for the parameters of the 10-GeV measurements. Figures 5(a) and 5(b) show spectra measured at low beam intensity for roughly the conditions of the 10- and 14-GeV measurements reported here. These spectra measurements, carried out with a pair spectrometer as discussed in Ref. 4, were difficult owing to the poor duty cycle of the SLAC beam, which makes coincidence measurements troublesome. This ruled out continuous monitoring of the spectra in this way.

The diamond was held in the SLAC goniometer as illustrated schematically in Fig. 6. The angular orientation is parametrized by two small rotation angles θ_H and θ_V. For simplicity in the discussion we assume that (1, 0, 0) is precisely in the z direction and (0, 1, 1) in the y direction when θ_H and θ_V are zero.

For a particular reciprocal lattice vector $(0, k, l)$, q_z is zero when $(l + k)\theta_H = (l - k)\theta_V$. For such an orientation of the diamond the coherent radiation consists of a large number of soft photons, and the ratio of the number flux of produced photons to their energy flux shows a pronounced maximum. This maximum lies along a line in θ_H, θ_V space; it would be a ridge on a contour map. Experimentally these ridges are mapped out by the "thin/thick" method[10] using two photon beam monitors, one sensitve to the number of photons above some threshold ("thin") and the other to the total energy ("thick"). Control of the goniometer was channeled through the on-line computer, which enabled these otherwise laborious thin/thick ridge maps to be made automatically by the computer. The procedure was to fix either θ_H or θ_V at a value as large as the goniometer would allow and take a series of short beam monitor runs while varying the other angle. Ridge profile curves were used to determine the precise alignment of the diamond. The position of the maximum could be located to an accuracy of one goniometer motor step or 23 μrad. In addition, the width of the curves was an important indicator of diamond quality, which

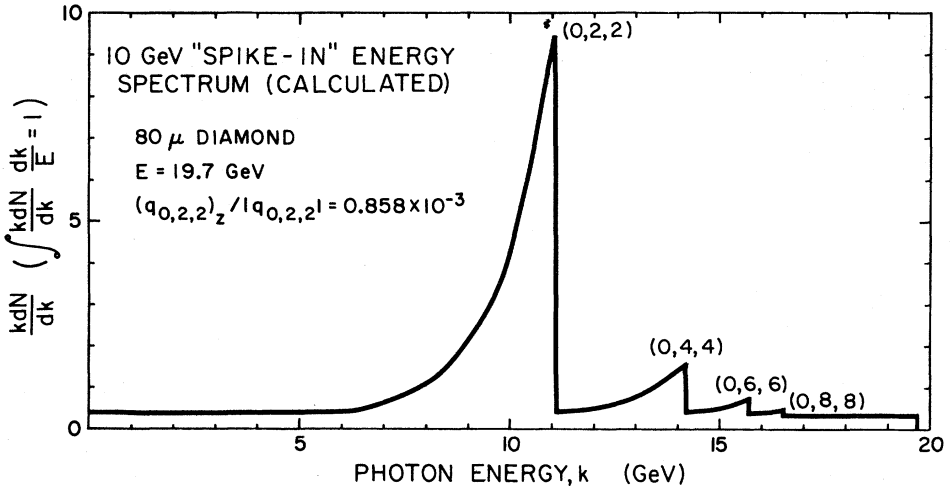

FIG. 4. Calculated intensity distribution for the 10-GeV setting of the CCB setup.

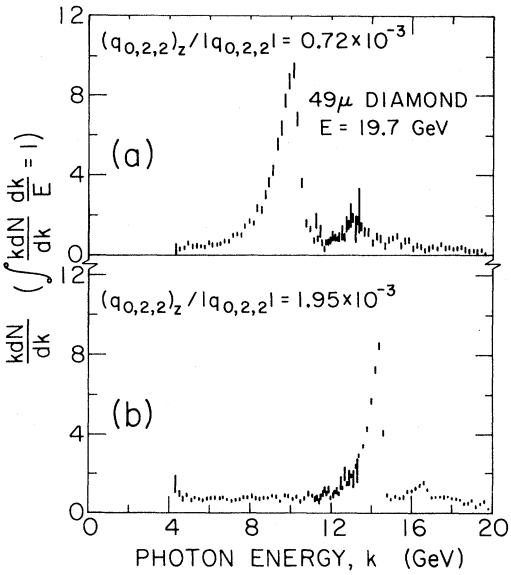

FIG. 5. (a) Measured intensity distribution of the 10-GeV setting; (b) measured intensity distribution of the 14-GeV setting.

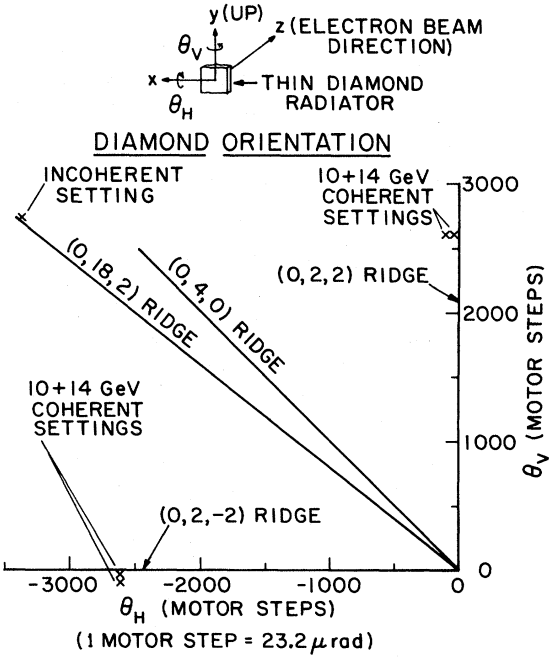

FIG. 6. Angular map of diamond settings. $\theta_H = \theta_V = 0$ corresponds to (1, 0, 0) in the z direction, (0, 1, 1) in the y direction.

was being continously degraded by radiation damage during the experiment. Examples of ridge profiles are shown in Fig. 7.

The diamond orientations used in this experiment are shown in Fig. 6. For the coherent settings, the angular distance from the (0, 2, 2) ridges determines the main spike energy. The linear polarization (the $\vec{E}$ vector) of the coherent radiation tends to be in the direction of the momentum transfer $\vec{q}$. The (θ_H, θ_V) settings near the (0, 2, 2) ridge give vertical polarization of the coherent radiation spike, and those near the (0, − 2, 2) ridge give horizontal polarization. A run with either of these settings is denoted by the term "spike in."

When the goniometer setting was such that the angular distance from the strongest ridges was large, the spectrum consisted mainly of incoherent radiation, which is very similar to ordinary bremsstrahlung from an amorphous or polycrystalline radiator; this setting was called "spike out." For the spike out, nominally incoherent setting used in the experiment, the remnant coherent radiation was quite small. However, we did find some indirect experimental evidence for small coherent contributions from the (0, 4, 0) and (0, 18, 2) ridges.

B. CCB subtraction method

To obtain the cross section for photons with the energy of the coherent spike one must subtract the measured yields from spike-in and spike-out runs with suitable relative normalization. Experimentally, what is available is (a) "spike in," the total yield Y_{in} from coherent plus incoherent radiation and corresponding integrated incident energy flux I_{in}, and (b) "spike out," the yield from incoherent radiation Y_{out} and corresponding incident energy,

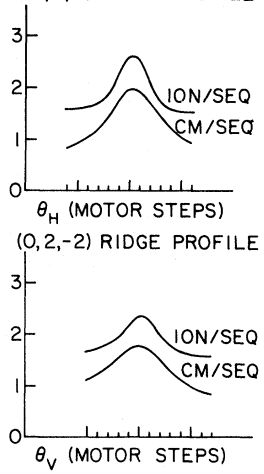

FIG. 7. Examples of "thin/thick" profiles—intensity-ratio curves which established crystal orientation. The maximum of the curve corresponds to $\vec{q}$ (0, 2, ±2) perpendicular to the average electron-beam direction. One motor step is 23.2 μrad. The rates ION and CM are proportional to the number of incident photons and the SEQ rate is proportional to the energy of the incident photons. The peak corresponds to the production of a high intensity of low-energy photons.

I_{out}. To subtract the incoherent contribution we need (c) the experimentally determined quantity α, roughly the ratio of coherent energy to incoherent energy in the beam with spike in, as explained below. Finally, to compute a cross section per incident photon we need (d) the average energy $\bar{k}$, a calculated quantity referring to the effective energy spectrum after subtraction.

The basis of the method used to subtract the incoherent yield was the assumption that the incoherent part of the energy spectrum was independent of crystal orientation. This reasonable expectation (the angular range involves only a few mrad) was verified to a certain extent by the measurements described in Ref. 4. With this assumption, the number of incoherent photons produced is exactly proportional to the number of electrons incident on the diamond. Thus, yields from spike-in and spike-out runs, normalized to equal numbers of incident electrons and subtracted, give the yield from an effective, entirely coherent spectrum.

As noted above, very precise monitors of the primary electron beam intensity were available at SLAC, the "toroids." Toroids could not be directly used for beam normalization because only some fraction (about 70%) of the electron beam actually passed through the diamond and this fraction was not perfectly stable. The electron beam optics were such that the beam was large at the position of the diamond and converged toward a small spot at the 2-mm primary collimator, thus effectively focusing the bremsstrahlung on the collimator. At times, use of the highest possible intensity of the electron beam was necessary to provide adequate photon beam intensities. The large power levels ruled out collimation of the electron beam to the size of the diamond, aside from a one-sided collimation to shadow the diamond's support structure. At reduced electron beam intensities it was possible to collimate the electron beam closely, and this was occasionally done as part of the special measurements described below.

Since the toroid was not a valid long-term monitor of the photon beam, we used a special measurement to relate the toroid to the SEQ, our primary beam monitor, and to determine the subtraction parameter α. Measurement of α consisted of a series of short beam monitor runs with the goniometer alternating rapidly back and forth between spike-in and spike-out settings:

$$1+\alpha=\frac{(\mathrm{SEQ/toroid})_{in}}{(\mathrm{SEQ/toroid})_{out}} \quad . \tag{2}$$

The validity of an SEQ/toroid measurement depended upon its reproducibility; we required that either two spike-out values repeated, bracketing the spike-in measurement, or vice versa.

Measurements of α were also made with a small electron beam constrained to intercept the diamond, produced by close collimation of the electron beam at greatly reduced power levels. These measurements repeated very well and generally agreed with those obtained by the first procedure above. However, the first procedure was less susceptible to systematic errors arising from possible nonuniformity of the diamond and was adopted as standard.

The formula for the yield per incident energy after subtraction of the incoherent part is easily written down if we first assume that a monitor of the electron beam is available. Letting T stand for the number of incident electrons, the result is

$$\frac{(Y/T)_{in}-(Y/T)_{out}}{(I/T)_{in}-(I/T)_{out}}=(Y/I)_{in}\left(1-\frac{(Y/I)\ /(Y/I)_{in}-1}{\alpha}\right). \tag{3}$$

The right-hand side of the above equation, involving the parameter α, is obtained from the left-hand side using the definition of α, Eq. (2).

The measurements reported here utilized an 80-μthick diamond. This diamond was used for approximately 2×10^{19} incident electrons and was then reused after an annealing process to remove radiation damage. α had the value 2.07 ± 0.08 for the 10-GeV goniometer setting and 0.58 ± 0.02 for the 14-GeV setting.

The complete formula for the measured cross section per incident photon involves the average energy $\bar{k}$ defined by

$$\bar{k}=\int k\,\frac{dN_{eff}}{dk}\,dk\Big/\int\frac{dN_{eff}}{dk}\,dk \ . \tag{4}$$

Here dN_{eff}/dk is the effective photon spectrum after subtraction:

$$\frac{dN_{eff}}{dk}=\frac{dN_{in}}{dk}-\frac{dN_{out}}{dk}\ , \tag{5}$$

where $(dN_{in,\ out}/dk)dk$ is the number of photons in energy range dk per incident electron for the spike-in and spike-out crystal orientations, respectively.

The formula for the cross section is

$$\sigma_{exp}=\bar{k}(Y/I)_{in}\left(1-\frac{(Y/I)_{out}/(Y/I)_{in}-1}{\alpha}\right) \ . \tag{6}$$

In terms of the effective energy spectrum and the actual cross section $\sigma(k)$ as a function of energy at fixed laboratory momentum and angle, σ_{exp} is given as follows:

$$\sigma_{exp}=\int\sigma(k)\,\frac{dN_{eff}}{dk}\,dk\Big/\int\frac{dN_{eff}}{dk}\,dk \ . \tag{7}$$

Thus, for a linear dependence of $\sigma(k)$ on k, σ_{exp} is exactly $\sigma(\bar{k})$. For the single-particle inclusive process measured in this experiment, the effect of nonlinear energy dependence was estimated to be of the order of 1%.

$\bar{k}$ was calculated using the formulas for the coherent spectrum given in Appendix A. This requires some attention to higher-order spikes in the spectrum, even for the nominal spike-out setting. We calculated the spike energy and approximate spike intensity from all reciprocal lattice vectors $(0, k, l)$ with k and l in the range ± 50. The result was that higher-order spikes contribute to the spectrum an amount of energy $0.08^{+0.08}_{-0.04}$ times the incoherent energy. However, all of the higher-order spikes occur near the end-point energy. The results for $\bar{k}$ were 9.85 ± 0.10 GeV and 13.8 ± 0.4 GeV for the nominal 10- and 14-GeV spectra.

From Eq. (6), the sensitivity of the subtracted cross section to errors in α depends on the ratio of spike-out yield per incident energy, $(Y/I)_{\text{out}}$, to the spike-in yield per incident energy, $(Y/I)_{\text{in}}$. The yield ratio was in the range 1–1.5 for the bulk of our 10-GeV data. For our low-momentum (0.5 GeV/c) π^+ runs we were sensitive to incident γ rays with energies as low as 0.6 GeV. For these runs the yield ratio climbed into the range 1.5–2. In the worst case of a yield ratio of 2, the uncertainty in our measurement of α produced only a $\pm 3.6\%$ uncertainty in the value of the subtracted cross section. This uncertainty has been added in quadrature to the error in our final result.

IV. DATA ANALYSIS

For each accumulation of event data for a particular spectrometer and goniometer setting (run), a yield per unit incident energy was calculated using the integrated photon beam intensity as normalization. The normalized yields from full-target and empty-target runs were subtracted (empty-target rates from 1% to 8%) and the spike-in and spike-out results then combined to produce the final cross section using Eq. (6).

Good events were required to have an unambiguous pattern in the P, θ, and ϕ hodoscopes and to have the initial vertical projected angle ϕ_0 within a certain range, slightly larger than the 60-mrad angular opening of the spectrometer entrance slits. Particles counting in the Čerenkov counter were called pions and those not counting were called protons. The yield was corrected for detection inefficiencies, decay losses (for pions), absorption and scattering in the counters, and a background to be discussed below.

Particle identification with the Čerenkov counter was based on the assumption that the number of kaons could be neglected. The assumption of a small kaon contribution is based on the following arguments. Previous measurements of particle production from pp collisions[3] show that the K/π ratio is on the order of 5% at these energies, and because of the short lifetime of the kaon only about one-half of the kaons, at most, survive to reach the spectrometer detectors. For momenta of 0.9 GeV/c and below, kaons should be discernible in our experiment at the few-percent level, using TOF and wall-counter pulse-height information together with that from the Čerenkov counter; no signal was seen. By looking at the Čerenkov counter inefficiency as a function of angle for negative polarity momentum settings, assuming that the number of $\bar{p}$'s is negligible, we had an independent check that the K^- signal was small.

Corrections for losses due to computer logging deadtime (less than 15%), ambiguous hodoscope patterns (typically 6%), and fast-electronics deadtime (typically 1% or less) were made on a run-to-run basis. The other corrections were momentum-dependent but otherwise applied uniformly to all the data.

The corrections for decay loss, absorption, and scattering were calculated using a Monte Carlo simulation of the spectrometer. The correction for the loss of particles by interactions in the counters was tested by a set of runs with and without an additional 1-in. thickness of Lucite at the ϕ hodoscope. The Monte Carlo program agreed well with these measurements.

The background was discovered by studying the distributions of reconstructed initial vertical angle. These were expected to reflect the 60-mrad opening of the slits, broadened slightly by the effects of finite resolution, decay, and scattering. The measured distributions were found to have tails not present in the Monte Carlo simulations. The apparent source of these tails was scattering and secondary production in the aluminum walls of the spectrometer vacuum chamber. These tails were extrapolated smoothly through the ϕ_0 distributions to estimate the background contribution. In this way a correction was obtained, varying from 6% at 1.5 GeV/c momentum to 9% at 0.5 GeV/c momentum. The uncertainty in this correction was taken to be one-half the value of the correction.

For the pion data the over-all momentum-dependent correction was approximately constant due to the opposite momentum dependence of the component factors. Its value was approximately 1.15 with an estimated uncertainty of 0.04 to 0.06.

Additional nonstatistical uncertainties were assigned to the data because of the errors in α and $\bar{k}$, the spectrum parameters appearing in Eq. (6).

These were propagated in a straightforward way and added in quadrature with the statistical errors.

V. RESULTS

Our results are given in Table I, for 10 GeV photon energy, and Table II, a 10- and 14-GeV comparison. As already discussed, the stated errors include other sources of error besides counting statistics. In Tables I and II and throughout this paper, the cross section is measured in units of the total photon-proton hadronic cross section, σ_{tot}, taken as 1.2×10^{-28} cm^2 for both 10

TABLE I. Single-particle production by 9.85-GeV linearly polarized photons (polarization = 60%) incident on hydrogen. $\parallel$ and $\perp$ refer to the beam polarization being parallel or perpendicular to the production plane. Entries are the invariant cross section, averaged over polarization, divided by $\sigma_T = 0.12$ mb, and multiplied by 100.

Particle type	x[b]	P_T (GeV/c)	$\left(\frac{100}{\sigma_T}\right)\frac{Ed\sigma}{d^3p}$ (GeV^{-2})	$\frac{\sigma_\parallel-\sigma_\perp}{\sigma_\parallel+\sigma_\perp}$ (%)	Particle type	x[b]	P_T (GeV/c)	$\left(\frac{100}{\sigma_T}\right)\frac{Ed\sigma}{d^3p}$ (GeV^{-2})	$\frac{\sigma_\parallel-\sigma_\perp}{\sigma_\parallel+\sigma_\perp}$ (%)
π^+	−0.32	1.017	0.328 ± 0.016 [a]		π^-	−0.32	1.017	0.178 ± 0.008 [a]	
		0.866	0.944 ± 0.045	0.4 ± 2.5			0.866	0.533 ± 0.026	0.8 ± 2.7
		0.706	2.63 ± 0.15	−0.1 ± 2.5			0.706	1.534 ± 0.085	2.6 ± 2.5
		0.589	5.32 ± 0.29 [a]				0.589	3.14 ± 0.18	6.2 ± 3.0
		0.458	10.47 ± 0.74 [a]				0.458	5.90 ± 0.38	−1.8 ± 2.9
	−0.24	0.938	0.700 ± 0.031 [a]			−0.24	0.936	0.429 ± 0.020 [a]	
		0.795	1.821 ± 0.086	−0.7 ± 2.3			0.795	1.119 ± 0.055	−1.7 ± 2.8
		0.646	4.53 ± 0.25	−0.3 ± 2.4			0.645	3.09 ± 0.18	2.7 ± 2.9
		0.539	8.33 ± 0.48	0.9 ± 2.6			0.539	5.63 ± 0.32	−1.5 ± 2.6
		0.422	17.8 ± 1.3	−5.3 ± 2.3			0.422	10.57 ± 0.69	0.8 ± 2.8
	−0.16	0.843	1.500 ± 0.073	−0.1 ± 2.7		−0.16	0.843	0.987 ± 0.044 [a]	
		0.710	3.79 ± 0.18	−1.2 ± 2.2			0.710	2.42 ± 0.12	1.5 ± 2.5
		0.571	9.40 ± 0.52	1.6 ± 2.4			0.571	6.83 ± 0.36	2.6 ± 2.0
		0.474	17.4 ± 1.0	3.4 ± 2.8			0.474	11.61 ± 0.64	4.0 ± 2.4
		0.369	32.4 ± 2.2	−3.7 ± 2.5			0.369	22.2 ± 1.4	2.7 ± 2.7
	−0.08	0.734	3.47 ± 0.17	−0.4 ± 2.5		−0.08	0.734	2.46 ± 0.11 [a]	
		0.605	8.41 ± 0.40	−3.8 ± 2.2			0.605	6.08 ± 0.28	2.4 ± 2.0
		0.476	19.5 ± 1.1	−2.9 ± 2.7			0.476	14.37 ± 0.74	1.7 ± 1.5
		0.385	37.7 ± 2.1	0.2 ± 2.6			0.386	25.2 ± 1.4	3.1 ± 2.4
		0.292	63.2 ± 4.1	−0.8 ± 2.0			0.292	44.2 ± 2.8	2.0 ± 2.7
	0.00	0.593	9.50 ± 0.45	−3.5 ± 2.4		0.00	0.593	7.21 ± 0.32 [a]	
		0.469	22.6 ± 1.0	3.6 ± 1.9			0.469	17.80 ± 0.80	4.2 ± 1.9
		0.341	53.5 ± 2.9	0.6 ± 2.0			0.341	39.1 ± 2.1	2.1 ± 1.9
		0.253	98.0 ± 5.2	−0.3 ± 1.9			0.253	80.2 ± 4.2	3.7 ± 2.1
		0.157	156.0 ± 9.9	0.2 ± 2.6			0.157	119.6 ± 7.4	−0.6 ± 2.5
	0.04	0.371	45.4 ± 2.1	−1.0 ± 2.0		0.04	0.371	36.5 ± 1.6	5.3 ± 1.7
	0.06	0.463	25.1 ± 1.2	−1.0 ± 2.1		0.06	0.463	18.47 ± 0.85 [a]	
p	−0.60	1.017	1.066 ± 0.069 [a]		p	−0.81	0.589	12.02 ± 0.81 [a]	
	−0.52	0.938	1.92 ± 0.12 [a]			−0.73	0.539	15.1 ± 1.1	−0.9 ± 2.7
	−0.44	0.843	3.18 ± 0.21	−3.6 ± 1.9		−0.65	0.474	22.8 ± 1.9	−6.6 ± 3.6
	−0.36	0.734	5.31 ± 0.36	−0.3 ± 2.0		−0.57	0.385	29.8 ± 2.7	−10.5 ± 4.5
	−0.28	0.593	9.05 ± 0.63	0.3 ± 2.4		−0.49	0.253	43.5 ± 4.1	−2.5 ± 4.8
	−0.22	0.463	12.61 ± 0.92	−0.1 ± 3.0		−0.82	0.422	34.2 ± 2.5	−0.2 ± 2.5
	−0.65	0.866	2.54 ± 0.17	0.2 ± 1.6		−0.74	0.369	43.4 ± 3.5	1.3 ± 3.1
	−0.57	0.795	4.01 ± 0.27	−3.7 ± 1.8		−0.66	0.292	59.4 ± 5.8	−12.3 ± 3.8
	−0.49	0.710	6.64 ± 0.45	−2.4 ± 1.9		−0.58	0.157	85.0 ± 11.0	−1.8 ± 7.3
	−0.41	0.605	10.73 ± 0.74	0.8 ± 2.2					
	−0.33	0.469	16.2 ± 1.2	−0.1 ± 2.6					
	−0.29	0.371	21.1 ± 1.6	−1.8 ± 3.6					
	−0.73	0.706	5.31 ± 0.36	−0.5 ± 2.2					
	−0.65	0.646	8.48 ± 0.59	1.6 ± 2.3					
	−0.57	0.571	13.34 ± 0.96	−0.5 ± 2.5					
	−0.49	0.476	18.5 ± 1.5	−0.1 ± 3.5					
	−0.41	0.341	30.4 ± 2.4	0.6 ± 3.6					

[a] $\perp$ polarization only. [b] $x = P_L^*/P_0$, where P_0 is the initial c.m. momentum.

TABLE II. Dependence of inclusive cross section on photon beam energy.

Particle type	x	P_T (GeV/c)	$\left(\frac{1}{\sigma_{tot}}\right)\frac{Ed\sigma}{d^3p}$ (GeV^{-2}) [a] $k=9.85$ GeV	$k=13.8$ GeV	Ratio
π^+	0	0.5	0.1856 ± 0.0080	0.182 ± 0.011	0.98 ± 0.07
	0	0.4	0.339 ± 0.017	0.368 ± 0.024	1.09 ± 0.09
	0	0.3	0.710 ± 0.039	0.670 ± 0.048	0.94 ± 0.08
π^-	0	0.5	0.1489 ± 0.0065	0.1440 ± 0.0087	0.97 ± 0.07
	0	0.4	0.292 ± 0.015	0.261 ± 0.017	0.90 ± 0.07
	0	0.3	0.517 ± 0.026	0.518 ± 0.035	1.00 ± 0.08
p	−0.28	0.5	0.133 ± 0.008	0.1146 ± 0.0098	0.86 ± 0.09
	−0.33	0.4	0.204 ± 0.015	0.180 ± 0.019	0.88 ± 0.11

[a] $\sigma_{tot} = 1.2\times10^{-28}$ cm^2.

and 14 GeV. The single-particle inclusive cross section expressed in this way, when integrated over invariant phase space, gives the multiplicity or average number of particles of that type produced.

In Table I the polarization asymmetry $(\sigma_{\parallel}-\sigma_{\perp})/(\sigma_{\parallel}+\sigma_{\perp})$ refers to the asymmetry actually observed as the linear polarization was changed from being predominantly parallel to the particle production plane ($\parallel$) to being perpendicular to it ($\perp$). The true asymmetry of the cross section would be obtained by dividing this quantity by the beam polarization $P=(N_{\parallel}-N_{\perp})/(N_{\parallel}+N_{\perp})$. Using the formulas given in Appendix A the average beam polarization was calculated to be 0.60 for the 10-GeV spectrum.

Figure 8 shows the location of the 10-GeV data points in $x-P_T$ space or equivalently in c.m. momentum. The photon can be thought of as incident from the left and the target proton from the right. Our measurements were at negative x, the target fragmentation region, and at $x=0$. The 14-GeV points were at $x=0$ only. Data for both particle signs were obtained in all cases.

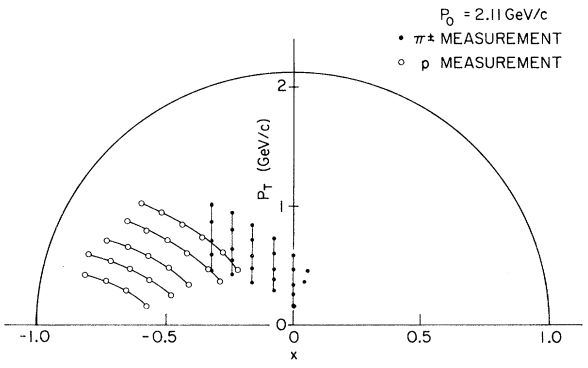

FIG. 8. Spectrometer settings for which data was obtained, plotted as x-P_T points (or equivalently, c.m. momentum), for 10-GeV photons. Only points at $x=0$ were obtained for 14-GeV photons. Data were obtained for both particle signs in all cases. $x=P_L^*/P_0$, where P_0 is the initial c.m. momentum.

The data points in Fig. 8 represent a set of spectrometer measurements for laboratory momenta of 1.5, 1.2, 0.9, 0.7, and 0.5 GeV/c and laboratory scattering angle such that x for a detected pion was equal to −0.32, −0.24, −0.16, −0.08, and 0. For each such spectrometer setting, the x value for a detected proton is shifted toward more negative values.

The lines shown in Fig. 8 represent the domains of one-dimensional interpolating fits that were made to the data. For pions, these lines correspond to constant x; for protons, to constant laboratory momentum. In both cases the fitting function was a three-parameter function of the form $\exp(A-BP_T-CP_T^2)$. For pions these constant-x fits are shown in Figs. 9 and 10. By a linear interpolation (in x for example) of the fitted value of $\log(Ed\sigma/d^3p)$ from line to line, $Ed\sigma/d^3p$ was ob-

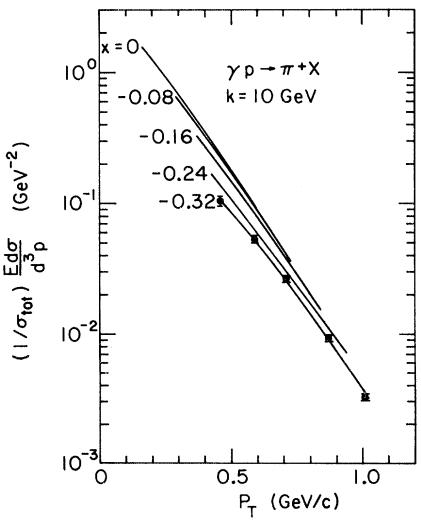

FIG. 9. Results of fitting the data with a smooth function of P_T, at each x, for π^+.

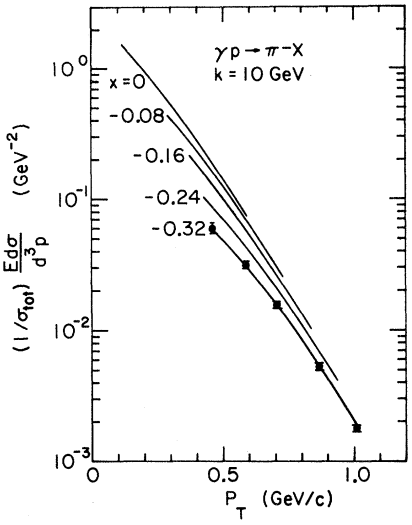

FIG. 10. Same as Fig. 9 but for π^-.

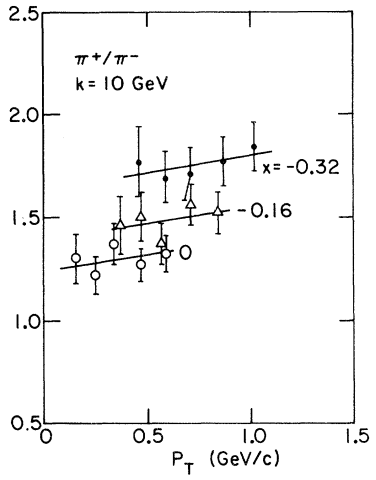

FIG. 11. π^+/π^- ratio as function of transverse momentum, for different x values (k = 10 GeV).

tained at points x, P_T not directly measured for the comparisons discussed below.

VI. DISCUSSION

Transverse momentum dependence. The measured cross sections, normalized by the total cross section, for π^+ and π^- are plotted as a function of P_T for various x values in Figs. 9 and 10. The falloff in P_T is approximately $\exp(-P_T/0.15$ GeV). There is a suggestive similarity in the shapes of the curves for different x values, but it is not close enough to allow the data to be represented by a product of two functions, one depending only on P_T and the other only on x.

Ratio of π^+ to π^- production. Figure 11 shows the π^+/π^- ratio as a function of P_T for various x values. The P_T variation is small but the ratio increasingly favors the π^+ at larger negative x. The ratio is ~1.3 at $x=0$ and ~1.75 at $x=-0.32$.

Rapidity dependence. Figure 12 shows the measured cross sections normalized by the total cross section as a function of rapidity, $y=\frac{1}{2}\ln[(E^*+P_L^*)/(E^*-P_L^*)]$ for various P_T. This distribution does show signs of flattening at the center of mass of the collision, $y=0$. However, no extended central region has developed at 10 GeV.

Energy dependence. In Table II we have listed the ratios of the cross sections at 10 and 14 GeV at $x=0$ for the π's, and at $x=-0.3$ for the protons. The $\pi^\pm$ cross sections show no change in value within our experimental limits of ±10%. The p cross section falls slightly at the higher energy. To show the energy dependence of the π^- cross section over a larger range, we have plotted in Fig. 13 the normalized cross sections as a function of incident photon energy for various P_T. The lower-energy points are obtained from the bubble-chamber data of Moffeit *et al.*[2] The two sets of data[11] join together in a reasonably smooth fashion. The distinct increase with energy of the lower-energy is presumably a threshold effect. The scaling we observe in our energy range is consistent with the behavior of the pion-produced inclusive pion cross sections.[12] The decrease of proton production with energy is also consistent with the pion-produced proton cross sections of Delay *et al.*[12]

Polarization dependence. The polarization asym-

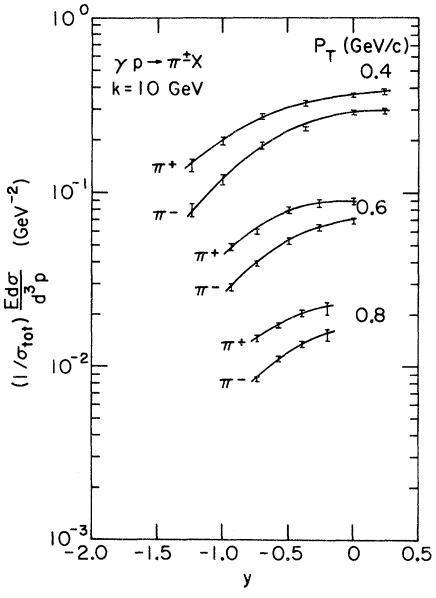

FIG. 12. Differential pion cross sections as a function of center-of-mass rapidity, y. Smooth curves have been added to guide the eye.

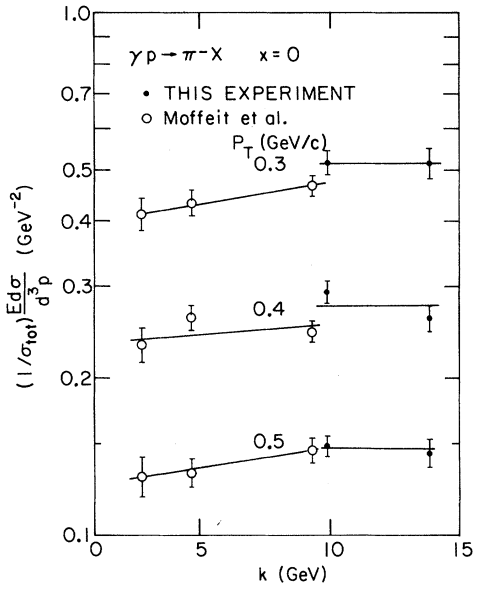

FIG. 13. Energy variation of the π^- cross section. The points at 2.8, 4.7, and 9.3 GeV are obtained from Ref. 2 by interpolation. Straight lines, horizontal in the case of our experiment, have been added to guide the eye.

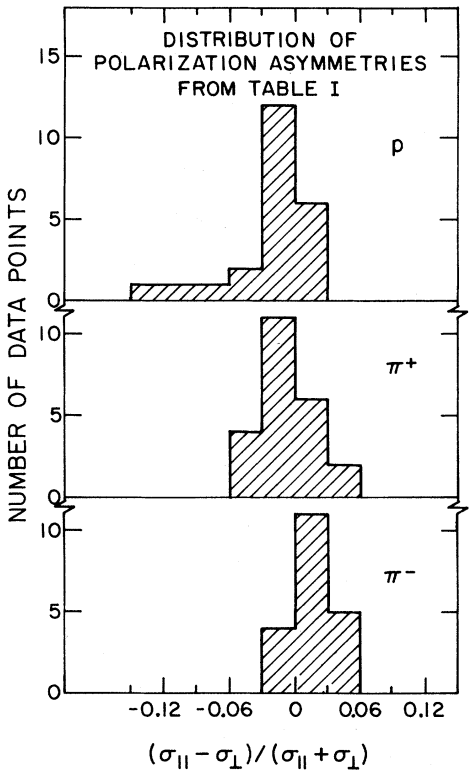

FIG. 14. Histogram of observed asymmetries, $(\sigma_{\parallel} - \sigma_{\perp})/(\sigma_{\parallel} + \sigma_{\perp})$, not corrected for the incomplete polarization of the beam, for pions and protons from 10-GeV photons.

metry listed in Table I is consistent with no polarization effect to about 3%, for the pions. The bulk of the proton data is also consistent with no polarization effect. However, in the kinematical region corresponding to a missing mass of ~2.3 GeV, the polarization asymmetry is (20 ± 6)% (using 0.6 for the beam polarization). Recoil protons from photons with polarization perpendicular to the production plane are favored. This effect is similar to the observed asymmetry in the photoproduction of pseudoscalar mesons.[13]

In order to contrast the size of the proton asymmetry with the fluctuations of our measurements, we have made histograms of the asymmetry for p, π^+, and π^- (see Fig. 14). The π^+ and π^- distributions are good approximations of Gaussians centered about zero asymmetry while part of the proton data shows a distinct asymmetry.

Comparison with p-p reactions. We have compared our measured cross sections for p, π^+, and π^- production with those from p-p reactions at 12.5 GeV/c beam momentum[14] as functions of x and P_T. These cross sections, normalized by their respective total cross sections, are displayed in Figs. 15, 16, and 17. There are strong similarities in the shape and normalization of all the curves. The similarity is particularly striking in the case of p production, where there is a complicated dependence on x and P_T rather than the simple exponential falloff observed for $\pi^{\pm}$ pro-

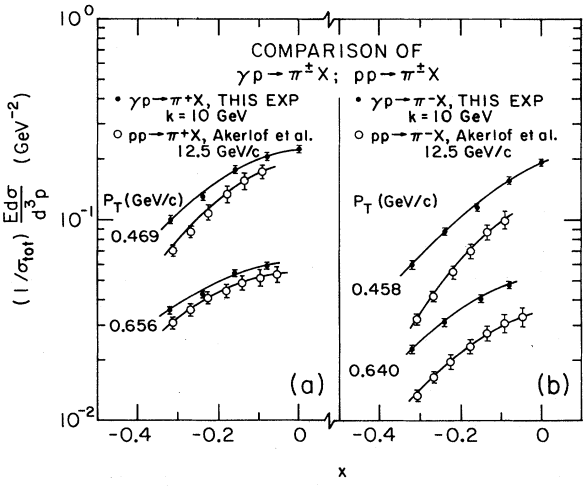

FIG. 15. Comparison of inclusive $\pi^{\pm}$ production from photons (this experiment) and from protons (Ref. 14) as a function of x. The invariant cross section is divided by the total cross section in each case. (a) π^+ production; (b) π^- production. The curves are added to guide the eye.

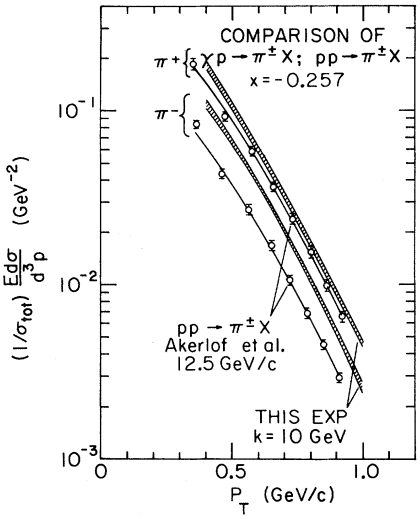

FIG. 16. Comparison of $\pi^\pm$ production from photons and protons, as in Fig. 15, but as a function of P_T. The curves are fits, to the actual data in the pp case, to interpolations in our case.

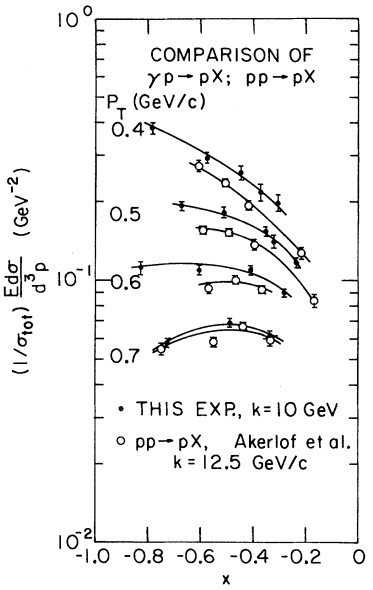

FIG. 17. Same as Fig. 15, for proton production.

duction.

The photoproduced hadrons always have a larger normalized cross section than the proton-produced hadrons. Roughly, the π^+ is 20% higher, the π^- is 70% higher, and p is 10% higher. The value assumed here for the ratio of the total cross sections is 325.

The relative cross sections are closer in value if the cross sections are normalized by their inelastic cross sections rather than the total cross sections. The inelastic cross section in p-p collisions at this energy is about $\frac{3}{4}$ of the total cross section. When inelastic cross sections rather than total cross sections are used for normalization, the p-p and γ-p cross sections generally differ by less than 25%

These similarities are expected in the context of projectile independence of target fragmentation[15]; it is notable that they occur so strongly at an energy as low as 10 GeV.

Comparison with earlier measurements. In Table III we compare the x and P_T dependence of our results for π^- with those of the bubble chamber experiment of Moffeit *et al.*[2] In our kinematical region, the differential cross sections measured by the bubble chamber represent averages over two large x bins (actually x'; see Appendix B), from to -0.1 and from -0.1 to -0.3, each divided into small P_T bins. The P_T dependence of the bubble chamber data for fixed x, the center of the bin, was fitted by our standard three-parameter function $\exp(A - BP_T - CP_T^2)$ to smooth the data and reduce fluctuations. Our data for comparison were interpolated to the same x value,

TABLE III. Comparison of this experiment (A) to the bubble-chamber experiment of Moffeit *et al.* and (B) for $\gamma p \to \pi^+ x$. The quantities shown are $10^3 \times (1/\sigma_{tot}) Ed\sigma/d^3p$. The bubble-chamber data are for 9.3 GeV photon beam energy and our data are for 10 GeV.

	$x = -0.049$			$x = -0.197$		
P_T (GeV/c)	A (GeV^{-2})	B (GeV^{-2})	A/B	A (GeV^{-2})	B (GeV^{-2})	A/B
0.2	827.0 ± 58.0	710.0 ± 30	1.16 ± 0.09			
0.3	465.0 ± 16.0	422.2 ± 9.9	1.10 ± 0.05			
0.4	251.3 ± 5.4	241.6 ± 6.9	1.04 ± 0.04	151.1 ± 6.0	117.9 ± 3.6	1.28 ± 0.06
0.5	130.7 ± 3.0	133.1 ± 4.7	0.98 ± 0.04	85.4 ± 2.1	74.5 ± 2.8	1.15 ± 0.05
0.6	65.4 ± 1.7	70.6 ± 2.8	0.93 ± 0.04	46.4 ± 1.2	44.2 ± 1.8	1.05 ± 0.05
0.7	31.5 ± 1.3	36.0 ± 1.9	0.88 ± 0.06	24.31 ± 0.61	24.6 ± 1.2	0.99 ± 0.05
0.8				12.26 ± 0.29	12.91 ± 0.93	0.95 ± 0.07
0.9				5.96 ± 0.24	6.35 ± 0.72	0.94 ± 0.11

using the procedure described above. The large bin size of the bubble chamber data in the variable x is estimated to make their result anomalously high by about 6% at $x=-0.2$ and a lesser amount at $x=-0.05$.

Broadly speaking, there is good agreement between the two experiments. However, it is evident that our results are systematically higher than those from the bubble chamber for lower P_T and more negative x. We were unable to explain this difference in terms of additional systematic errors in our measurement.

Comparison with the π^+ and π^- distributions in the projectile-fragmentation region. A DESY experiment[16] has measured the single-particle distributions in the projectile-fragmentation region in $\gamma p \to \pi^{\pm} X$ at $k=6$ GeV. The distributions in this experiment have similarities to the ones found in our experiment and are consistent with a smooth variation between the target- and projectile-fragmentation regions.

(a) *The ratio of π^+ to π^- production.* The π^+ production is always larger than the π^- production for both experiments. For $x=0.24$ in the DESY experiment, the π^+/π ratio varies from 1.1 at $P_T=0.1$ GeV/c to 1.3 at $P_T=1.0$ GeV/c. This ratio is slightly smaller than our measured π^+/π^- ratio at $x=0$, and has the same P_T dependence. This ratio is consistent with the observed rise in the π^+/π^- ratio as x becomes more negative. (See Fig. 11.)

(b) *The P_T distribution at various x.* For P_T in the interval 0.4 to 1.0 GeV/c, the invariant cross section falls off like $\exp(-P_T/0.15\ \text{GeV}/c)$ for all the x observed in both the target and the projectile fragmentation regions. The falloff is always less steep at $P_T<0.4$ GeV/c.

VII. CONCLUSION

The most striking aspects of the data are (a) the close similarity in form between the differential cross section for particle production by photons and by protons, and (b) the quantitative agreement (to about 25%) of the π^+, π^-, and p production cross sections with those measured in pp collisions, when scaled by the total inelastic cross sections. Our measurements of the pion production cross section show essentially no dependence on energy between 10 and 14 GeV, and no effect of beam polarization. Cross sections for proton production, on the other hand, show a discernible energy and polarization dependence.

ACKNOWLEDGMENTS

We are grateful to the many people at SLAC who contributed in an indispensible way to make this experiment possible. Most of the equipment used in this experiment had been built previously by other groups at SLAC or was constructed for our experiment by the SLAC Spectrometer Facilities Group.

Of those individuals directly involved in the work described here, we should particularly like to thank the following: Charles K. Sinclair, who developed the idea of using collimated coherent bremsstrahlung and who was very largely responsible for its realization; David J. Sherden, for his tireless help on software and many other details of a spectrometer experiment at SLAC; Mike Browne, for design of beam monitors and other electronics; Roger Miller, for design and setup of the electron beam optics; Dieter Walz, for design of the pin-cushion monitor; Roy Schwitters, for help in recommissioning the goniometer; Bob Eisele, for collimator and beam monitor design; and Roy Wilkinson and David Chiang, for programming and help during the running of the experiment.

APPENDIX A

Here, for reference, we state the formulas used to compute the CCB energy spectrum.

Coherent and incoherent bremsstrahlung

The number of coherent photons produced in a crystal of thickness t, having energy in the range dx and azimuthal angle in the range $d\phi$, is given by the following formula:

$$\frac{dN_{\text{coh}}}{dx\,d\phi}=\frac{16\pi t Z^2\alpha^3 E}{V_a{}^2 m^4}\sum_i \frac{q_{iT}{}^2}{q_i{}^4}|S(\vec{q}_i)|^2\,|1-F(q_i)|^2\exp(-Aq_i{}^2)$$
$$\times\frac{1-x}{x^2(1+\theta^2)^4}\left\{(1+\theta^2)^2[(1-x)^2+1]-8\theta^2(1-x)\cos^2\phi\right\}. \tag{A1}$$

The notation is changed from that of the body of the paper: x refers to the energy of the photon in units of the electron beam energy E, and θ is the photon's angle with respect to the electron beam direction in units of m/E, with m the electron mass. α is $\frac{1}{137}$, Z is the atomic number, and V_a is the volume of a unit cell of the crystal. For diamond $V_a=a^3$ with $a=3.56\times10^{-8}$ cm.

For each term in the sum over reciprocal lattice vectors $\vec{q}_i$ the azimuthal angle is measured with

respect to $\vec{q}_{iT}$, the part of $\vec{q}_i$ transverse to the electron beam direction; and there is an energy-angle constraint depending on $\vec{q}_i$:

$$q_{iz} = \frac{m^2 x(1+\theta^2)}{2E(1-x)} \quad , \tag{A2}$$

where q_{iz} is the component of $\vec{q}_i$ along the electron beam direction.

$S(\vec{q}_i)$ is the structure factor defined by $S(\vec{q}) = \sum \exp(i\vec{q}\cdot\vec{a})$, where the sum extends over the ν atomic positions in a unit cell. For diamond, $\nu = 8$.

$F(q)$ is the atomic form factor. Values of $F(q)$ were obtained from a nine-parameter analytic function given in Ref. 17.

The factor $\exp(-Aq^2)$ is the probability that no phonons are emitted or absorbed during the bremsstrahlung process, that is, the probability that the crystal does not change its state of internal motion. Calculations are made using the Debye model of a simple isotropic crystal with the following result:

$$A = \frac{3}{2M\theta_0^3}\int_0^{\theta_D}\left(1+\frac{2}{e^{w/T}-1}\right)w\,dw = \frac{3}{4M\theta_D}\left[1+4\left(\frac{T}{\theta_D}\right)^2\frac{\pi^2}{6}+\cdots\right] , \tag{A3}$$

where θ_D is the Debye temperature, T is the temperature, and M is the mass of the atoms making up the crystal. Although diamond is a nonsimple anisotropic crystal, the values of θ_D are obtained by a fit to experimental data for the specific heat,[18] so this formula probably holds in some average sense. Equation (A3) gives the value $0.5\times10^{-9}\text{eV}^{-2}$ for diamond.

The relative numbers of produced photons with linear polarization parallel to $\vec{q}_{iT}$ and perpendicular to it are

$$\begin{aligned} N_{\parallel} &\sim \tfrac{1}{2}(1+1-x)^2(1+\theta^2)^2 - 8\theta^2(1-x)\cos^2\phi \\ &\quad - 8\theta^4(1-x)\cos^2\phi\sin^2\phi \ , \\ N_{\perp} &\sim \tfrac{1}{2}x^2(1+\theta^2)^2 + 8\theta^4(1-x)\cos^2\phi\sin^2\phi \ . \end{aligned} \tag{A4}$$

After integration over the angle ϕ, the polarization $(N_{\parallel}-N_{\perp})/(N_{\parallel}+N_{\perp})$ is

$$P(x) = \frac{2(1-x)}{(1+\theta^2)^2[(1-x)^2+1]-4\theta^2(1-x)} \tag{A5}$$

in agreement with a formula given in Ref. 9, the standard reference for coherent bremsstrahlung.

Equations (A1), (A2), (A4), and (A5) are valid as long as E, $E(1-x) \gg m$, $\theta \ll E/m$, and $q_i^2 \ll m^2$.

There is also an incoherent contribution to the radiation. The number of incoherent photons produced in energy range dx and angular range $d\theta$ is given by

$$\frac{dN_{\text{inc}}}{dx\,d\theta^2} = \frac{2\nu t Z(Z+\zeta)\alpha^3}{V_a m^2 x}\left[\left(\frac{1+(1-x)^2}{(1+\theta^2)^2}-\frac{4\theta^2(1-x)}{(1+\theta^2)^4}\right)\left(\ln M(x,\theta)-2\delta\frac{Z}{Z+\zeta}\right)+\frac{16\theta^2(1-x)}{(1+\theta^2)^4}-\frac{(1+1-x)^2}{(1+\theta^2)^2}\right] . \tag{A6}$$

When δ and ζ are set equal to zero, this formula is identical to that given by Schiff.[19] $\zeta = \log(1440Z^{-2/3})/\log(183Z^{-1/3})$ is a correction for the contribution to bremsstrahlung from the atomic electrons, necessary to get agreement with the standard radiation length formula

$$\frac{1}{X_0} = \frac{4\nu Z(Z+\zeta)\alpha^3}{V_a m^2}\ln(183Z^{-1/3}) \ . \tag{A7}$$

δ is the correction for coherence effects, defined by

$$\begin{aligned} \delta &= \int_0^{\infty}\frac{dq}{q}\,|1-F(q)|^2\exp(-Aq^2) \\ &= \tfrac{1}{2}\{e^u(1+u)[\ln(1/u)-0.577+u+\cdots]-1\}, \\ u &= A/B^2 \ . \end{aligned} \tag{A8}$$

Here and in Schiff's calculation, the atomic form factor is assumed to be of the form $F(q) = 1/[1+(\beta q)^2]$, with β equal to $111Z^{-1/3}/m$. For diamond, Eq. (A8) gives 1.02. The effect of the δ term for diamond is a uniform reduction of the incoherent radiation by about 15%.

The requirement $q^2 \ll m^2$ must be satisfied for the δ term to be valid. That is, $1/A \ll m^2$. There is, in addition, the requirement of complete screening:

$$\frac{m^2 x(1+\theta^2)}{2E(1-x)} \ll 1/\beta \ . \tag{A9}$$

The quantity $M(x,\theta)$ as given by Schiff is

$$\frac{1}{M(x,\theta)} = \left(\frac{mx}{2E(1-x)}\right)^2 + \left(\frac{1}{\beta m(1+\theta^2)}\right)^2 \ . \tag{A10}$$

Effect of collimation

Collimation to extremely small angles (of order m/E) is required if one is to improve the photon energy spectrum. The characteristic multiple scattering angle and beam divergence angle are in practice comparable to the collimation angle.

As a result, collimation does not sharply limit the photon's angle with respect to the electron beam direction. The collimator aperture is in effect smeared out by the multiple scattering of the incident beam in the crystal before radiation, and by the nonzero spot size of the electron beam at the position of the collimator.

For the purposes of calculation the electron beam spot at the collimator was assumed to have a circular shape with a Gaussian intensity distribution. The projected standard deviation σ_x was related to the electron beam optics, the size of the diamond, and the phase space of the electron beam.

The electron beam optics produced an effective focus at the collimator. At the position of the diamond, a distance D upstream, the beam had a horizontal and vertical size d, roughly corresponding to the size of the diamond. In this situation σ_x is determined from the phase space of the electron beam, A, by solution of the following two equations:

$$\sigma_x{}^2 + D^2\sigma_\theta{}^2 = (d/2)^2 ,$$
$$\pi\sigma_x\sigma_\theta = A . \tag{A11}$$

The overall smearing function $p(\theta)$ was calculated as a convolution of Gaussian beam spot size smearing, having standard deviation $\sigma_1 = \sigma_x/D(E/m)$ and smearing due to multiple scattering in the crystal. The latter took into account multiple scattering only if it occurred before radiation, assuming that the photons were produced uniformly throughout the thickness of the diamond. The resulting smearing function is

$$p(\theta) = \frac{1}{2\sigma^2}\left[\mathrm{Ei}\left(\frac{\theta^2}{2(\sigma^2+\sigma_1^2)}\right) - \mathrm{Ei}\left(\frac{\theta^2}{2\sigma_1^2}\right)\right],$$
$$\mathrm{Ei}(x) \equiv \int_x^\infty \frac{e^{-t}}{t}\,dt . \tag{A12}$$

σ is the standard deviation in projected angle (in units of m/E) produced by multiple scattering in the entire thickness of the crystal. Multiple scattering was the greatest source of collimator smearing.

The usual expression for multiple scattering gives $\sigma^2 = 2\pi t/\alpha X_0$, where t is the thickness of the crystal and X_0 the radiation length. Substituting for X_0 using (A7), this can be written as

$$\sigma^2 = \frac{8\pi\nu\alpha^2Z^2t}{m^2V_a}\ln(183Z^{-1/3}), \tag{A13}$$

where the logarithmic term has the numerical value 4.6. An exact calculation of multiple scattering was made using specific expressions for carbon of the atomic and nuclear form factors. The result was to replace the logarithmic factor in (A13) by 4.2. This value was used in the collimation calculations.

Smearing converts the collimation effect from a sharp cutoff in angular integrals at the collimation angle θ_c to a weighting by an acceptance function $A(\theta)$ in an integral over all angles. Since the smearing means physically that sometimes the collimator hole appears to the photons to be displaced, but its area is always the same, we must have

$$\int_0^\infty A(\theta)\,d\theta^2 = \int_0^{\theta_c{}^2} d\theta^2 = \theta_c{}^2. \tag{A14}$$

The function $A(\theta)$ was evaluated by numerically integrating the following:

$$A(\theta) = \int_0^{\theta_c{}^2-\theta^2} p(u)\,du^2 + \int_{(\theta-\theta_c)^2}^{(\theta+\theta_c)^2} p(u)\,du^2 \tan^{-1}\left(\frac{\{[\theta^2-(\theta_c-u)^2][(\theta_c+u)^2-\theta^2]\}^{1/2}}{\theta^2-\theta_c{}^2+u^2}\right). \tag{A15}$$

A graph of the acceptance function is shown in Fig. 18 for the parameter values $\theta_c = 0.42$, $\sigma_1 = 0.3$, and $\sigma = 0.51$ and 0.65.

Expressed in terms of the collimator acceptance function $A(\theta)$, the CCB energy spectrum dN/dx is as follows:

$$\frac{dN}{dx} = A(\theta_{\mathrm{coh}})\int_0^{2\pi} d\phi\,\frac{dN_{\mathrm{coh}}}{dx\,d\phi} + \int_0^\infty \frac{dN_{\mathrm{inc}}}{dx\,d\theta^2}A(\theta)\,d\theta^2 . \tag{A16}$$

The coherent bremsstrahlung probability given by Eq. (A1) is easily integrated over azimuthal angle, since this involves only $\int \cos^2\phi\,d\phi = \pi$. For the coherent part, with x and a particular reciprocal lattice vector given, the angle θ_{coh} is obtained from relation (A2) and the acceptance cal-

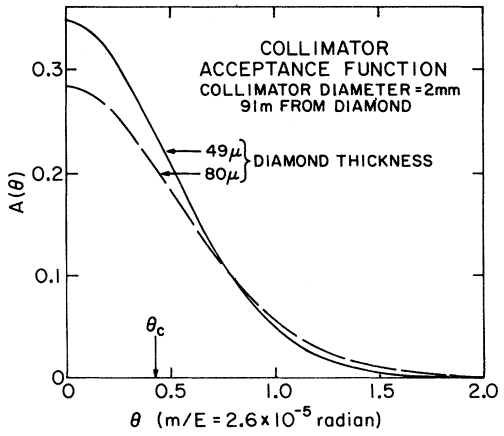

FIG. 18. Acceptance function for bremsstrahlung at the collimator, using the parameters of Appendix A.

culated for that value of θ. The incoherent part was evaluated by numerical integration using Eq. (A6).

APPENDIX B

Our choice of definition of the Feynman variable x used in this paper was motivated mainly by simplicity; it differs from a frequently used definition (x' below). All the various proposed "scaling variables" are equivalent in the high-energy limit and the difference, of order $1/s$, is usually neglected in Regge-Muller-type theories. However, at less than extreme high energy, particle production ratios and energy dependence can be substantially affected by choosing one or the other of these variables to hold constant. Here we show (to order $1/s$) the relation of two natural scaling variables describing the inclusive reaction $ab \to cX$ with particle masses M_a, M_b, and M_c. As usual, P_0 denotes the initial c.m. momentum, $s \sim 4P_0^2$, while $P_{0\,\max}$ is the maximum momentum available to the observed particle:

$$x = P_L^*/P_0 , \tag{B1}$$

$$x' = P_L^*/P_{0\,\max} \cong x\left(1 + \frac{M_c^2 + M_X^2 - M_a^2 - M_b^2}{s}\right), \tag{B2}$$

where M_X is the minimum allowed mass of the particle (or particles) X. Thus, if the $1/s$ term is negligible, holding either of these variables fixed (along with P_T) amounts to the same thing. However, for the energies involved in this experiment the $1/s$ term is not negligible. For example, for π production in pp collisions at 12 GeV/c, x' and x differ by almost 10%.

---

*Work supported in part by the National Science Foundation.

†Present address: Loyola Marymount University, 7101 W. 80th St., Los Angeles, California 90045.

‡Present address: Los Alamos Scientific Laboratory, Los Alamos, New Mexico 87544.

[1]M.-S. Chen *et al.*, Phys. Rev. Lett. 26, 1585 (1971).

[2]K. C. Moffeit *et al.*, Phys. Rev. D 5, 1603 (1972).

[3]Two recent compilations are A. N. Diddens and K. Schupmann, *Elementary Particle Properties and Production Spectra* in *Landolt-Börnstein: Numerical Data and Functional Relationships in Science and Technology*, edited by H. Schopper (Springer, Berlin, 1972) New Series, Vol. 6; M. Law *et al.*, LBL Report No. LBL-80, 1972 (unpublished).

[4]W. W. Ash *et al.* (unpublished).

[5]The coherent bremsstrahlung facility is described in R. Schwitters, SLAC Report No. SLAC-TN-70-32, 1970 (unpublished); R. Schwitters, thesis, M.I.T., 1970 (unpublished). The SLAC beam monitor toroids are described in R. Larsen and D. Horelick, SLAC Report No. SLAC-PUB-398, 1968 (unpublished); R. S. Larsen, SLAC Report No. SLAC PUB-947, 1971 (unpublished).

[6]G. Miller and D. Walz, SLAC Report No. SLAC-PUB-1297 (unpublished).

[7]R. Anderson *et al.*, Nucl. Instrum. Methods 66, 328 (1968).

[8]R. L. Anderson, Nucl. Instrum. Methods 65, 195 (1968).

[9]G. Diambrini Palazzi, Rev. Mod. Phys. 40, 611 (1968).

[10]D. Luckey and R. F. Schwitters, Nucl. Instrum. Methods 81, 164 (1970).

[11]For each point we averaged the logarithm of the cross sections of Ref. 2 over four symmetrically located bins.

[12]P. Bosetti *et al.*, Nucl. Phys. B54, 141 (1973); M. Delay *et al.* (unpublished).

[13]D. J. Sherden *et al.*, Phys. Rev. Lett. 30, 1230 (1973).

[14]C. W. Akerlof *et al.*, Phys. Rev. D 3, 645 (1971).

[15]R. P. Feynman, Phys. Rev. Lett. 23, 1415 (1969); J. Benecke, T. T. Chou, and C. N. Yang, Phys. Rev. 188, 2159 (1970); C. N. Yang, in *High Energy Collisions*, edited by C. N. Yang *et al.* (Gordon and Breach, New York, 1969), p. 509.

[16]H. Burfeindt *et al.*, Nucl. Phys. B74, 189 (1974).

[17]D. T. Cromer and J. T. Waber, Acta Crystallogr. 18, 104 (1965).

[18]W. De Sorbo, Chem. Phys. 21, 876 (1952).

[19]L. I. Schiff, Phys. Rev. 83, 252 (1951).